ACS APPLIED ENERGY MATERIALS

www.acsaem.org Article

Advanced Two-Dimensional/Zero-Dimensional Carbon Composite Nanofluids for Enhanced Optical and Photothermal Performance in Direct Absorption Solar Collectors

Mahbobeh Javidi and Mohammad H. Entezari*

Cite This: ACS Appl. Energy Mater. 2025, 8, 8442−8457

Read Online

ACCESS | Metrics & More | Article Recommendations | Supporting Information

ABSTRACT: Nanofluid is an ideal working fluid for direct absorption solar collectors (DASCs) and a promising technology for solar energy harvesting. An advanced composite of reduced graphene oxide (rGO) nanosheets and nitrogen-doped carbon quantum dots (N-CQD) was prepared by using a hydrothermal technique. The X-ray photoelectron spectroscopy (XPS) analysis confirmed the presence of N-CQD on the surface of rGO, resulting in the formation of a rGO/N-CQD composite. Additionally, transmission electron microscopy (TEM) analysis verified the uniform distribution of N-CQD on rGO nanosheets. Physicochemical property investigations reveal that the rGO/N-CQD$_{60/40}$ nanofluid exhibits the highest thermal conductivity (TC) with proper stability. An artificial neural network (ANN) was developed to estimate the TC of the rGO/N-CQD$_{60/40}$ nanofluid using temperature and concentration as inputs. The model accurately predicted the TC, achieving a coefficient of determination (R^2) of 0.9974. The composite of rGO/N-CQD$_{60/40}$ greatly enhances optical absorption compared to GO and N-CQD. The rGO/N-CQD$_{60/40}$ nanofluid, which achieves 82.64% photothermal conversion efficiency (η) at 1 Sun (1000(W/m^2)) irradiation, has high potential as a working fluid for DASCs. The study examined how different solar radiation intensities affect photothermal conversion, showing η values of 82.64, 66.73, and 51.11% for the rGO/N-CQD$_{60/40}$ nanofluid at 1, 2, and 3 sun, respectively.

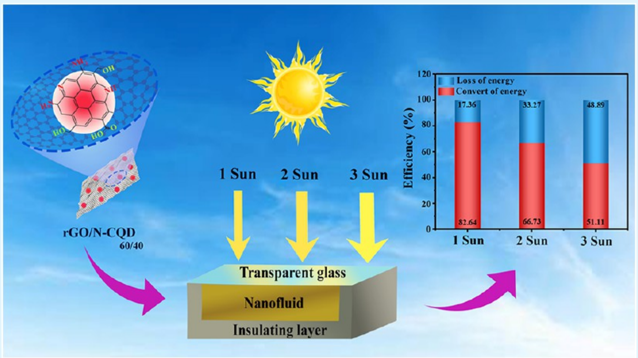

KEYWORDS: *rGO/N-CQD composite, nanofluid, direct absorption solar collector, photothermal conversion, thermal conductivity, artificial neural network*

Downloaded via Mohammad H. Entezari on June 28, 2025 at 20:54:37 (UTC).
See https://pubs.acs.org/sharingguidelines for options on how to legitimately share published articles.

1. INTRODUCTION

Rapid population growth and energy demands necessitate the development of renewable energy development. Fossil fuel dependence causes environmental issues, such as ozone depletion, air pollution, and climate change. Solar energy offers a promising, abundant, and clean alternative.[1,2] Solar energy applications encompass photothermal techniques, photovoltaics (PV), and photochemistry.[3] Solar thermal conversion is the most efficient method, transforming absorbed solar radiation into thermal energy.[4] Harnessing solar energy is increasingly important, as the Earth's surface receives more solar energy in 1 h than humanity consumes in a year.[5] Therefore, the efficiency (η) is critical for solar thermal applications. DASCs offer an alternative to surface absorption, directly heating the working fluid and minimizing temperature differences with the environment, thus boosting efficiency.[6] Conventional working fluids like oil, water, and ethylene glycol exhibit weak solar absorption, hindering the development of DASCs due to insufficient light capture and poor thermal conductivity. Nanofluids, with their adjustable optical absorption, offer significant promise for DASC applications.[7,8] Nanofluids' exceptional thermophysical properties, including high thermal conductivity,[9] heat transfer coefficients,[10] energy harvesting/storage,[11] solar evaporation,[12] and thermal diffusivities,[13] enhance DASCs efficiency. Furthermore, their sensitivity makes them valuable for monitoring DASC systems design modifications.[14] Nanoparticle addition enhances heat transfer via high thermal conductivity, but maintaining stability is crucial for optimal performance and viability as a working fluid. Studies demonstrate nanofluids' superior heat transfer capabilities in DASC systems.[15] Carbon nanostructures, possessing strong C−C bonds and low density, exhibit high TC.[16] Carbon, abundant on Earth, exists in various allotropes: 0D fullerenes,[17] 1D carbon nanotubes,[18] 2D graphene[19] have

Received: April 4, 2025
Revised: May 28, 2025
Accepted: June 4, 2025
Published: June 12, 2025

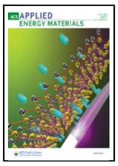

ACS Publications

© 2025 American Chemical Society

https://doi.org/10.1021/acsaem.5c00938
ACS Appl. Energy Mater. 2025, 8, 8442−8457

been experimentally synthesized. Graphene, an sp^2 hybridized carbon allotrope with a dense honeycomb structure, exhibits exceptional mechanical, electrical, electronic, and electrochemical properties, making it highly promising for materials science and scientific research.[20] Its micrometer-scale lateral size provides a large specific surface area and suitable aspect ratio for efficient heat carrier movement within its few-nanometer thickness. To minimize graphene nanoparticle sedimentation, even dispersion and stabilization are critical. Graphene nanofluid stability, vital for preparation, maintains a uniform particle distribution. Oxygen functionalization, while reducing the thermal conductivity of graphene derivatives relative to graphene, improves their stability.[21] Graphene oxide (GO)'s amphiphilic nature facilitates the formation of diverse and reactive nanostructures readily functionalized with nanoparticles. This functionalization modifies their thermophysical properties, enhancing nanofluid TC for improved performance in DASCs.[22] Nanocomposites with synergistic photothermal conversions are promising nanostructures. Carbon quantum dots (CQDs), novel 0D nanocarbon typically smaller than 10 nm, exhibit excellent characteristics, including low toxicity, versatile synthesis, water solubility, large surface area, and broad visible absorption. CQDs can be functionalized and doped with various elements (e.g., P, B, S, N) to improve solar energy absorption.[23] Their production relies on hydrothermal synthesis from small molecules at low temperatures, with heteroatom doping achieved through dopant precursor incorporation during synthesis.[24] Recent researches emphasize new materials and system optimization to improve efficiency and stability. For instance, ultrastable carbon quantum dot nanofluids have achieved >95% solar absorption and long-term stability in direct absorption solar collectors.[25] Studies also explore the synergistic effects of nanoparticles in composites to improve solar energy absorption efficiency, making them crucial for light-to-heat conversion. Chen et al. demonstrated 95.6% solar absorption efficiency with Cu@C nanoparticles in solar thermal conversion.[26] Furthermore, heterogeneous nanofluid studies show that nanoparticle distribution and volume fraction significantly impact local heating and solar thermal conversion efficiency.[27]

This study explores a novel aqueous nanofluid based on an rGO/N-CQD composite engineered to enhance photothermal conversion efficiency. By integrating the high TC of rGO nanosheets[28] with the excellence of N-CQD in DI water,[29] the composite is designed to achieve optimized thermophysical properties. The type, proportion, and synthesis conditions of the nanoparticles govern the composite's microscopic properties, which in turn significantly affect its macroscopic properties. Given the absence of prior research on rGO/N-CQD ratio optimization in nanofluids, this work provides valuable insights into the TC, stability, optical properties, and photothermal conversion performance of this stable carbon nanostructure composite for potential use in DASCs. An optimized ANN model has also been developed for accurate thermal conductivity prediction.

2. EXPERIMENTAL SECTION

2.1. Materials and Methods. GO nanosheets were prepared using a modified Hummers method with ultrasonic treatment (ROHS Ultrasonics, Korea), and N-CQD was synthesized via a hydrothermal method. A rGO/N-CQD nanocomposite, synthesized by a mild hydrothermal method, is proposed for DASC applications. The chemicals used in this study are listed in Table 1.

Table 1. Chemical Materials Utilized in This Study

chemical	purity (%)	supplier	role in synthesis
graphite (G)	99.9	Merck	precursor for GO synthesis
sulfuric acid (H_2SO_4)	98	Merck	oxidizing agent in Hummers method
phosphoric acid (H_3PO_4)	85	Merck	oxidizing agent in Hummers method
potassium permanganate ($KMnO_4$)	99	Merck	oxidizing agent in Hummers method
hydrogen peroxide (H_2O_2)	30	Merck	termination of oxidation
hydrochloric acid (HCl)	37	Merck	washing and purification
citric acid ($C_6H_8O_7$)	≥99.5	Merck	carbon source for N-CQD
ethylenediamine ($C_2H_8N_2$)	≥99	Merck	nitrogen doping agent for N-CQD
deionized (DI) water		lab-purified	solvent and washing

2.2. Synthesis of GO. GO was synthesized using an improved version of Hummers method in an ultrasonic bath at 40 kHz.[7] The process involved adding 0.5 g of G to a mixture of 7 mL of H_3PO_4 and 60 mL of H_2SO_4 in an ice bath. Subsequently, at a temperature of 18 °C, 3 g of $KMnO_4$ was added to the mixture, which was then sonicated for 20 min in an ultrasonic bath with a power of 150 W. Next, to dilute the mixture, 40 mL of DI water was gradually added to the suspension. The reaction was completed by adding an extra 100 mL of DI water and then 3 mL of H_2O_2 to the mixtures. The brown suspensions were washed multiple times with 120 mL of 10% HCl (v/v) and 120 mL of DI water to remove impurities. The resulting suspensions were centrifuged and dried for 12 h at 90 °C under a vacuum.

2.3. Synthesis of N-Doped CQD. N-doped CQDs were synthesized by dissolving 1.0507 g of $C_6H_8O_7$ and 335 μL of $C_2H_8N_2$ in 10 mL of DI water. The solution was heated in a 50 mL Teflon-lined autoclave at 150 °C for 5 h and then naturally cooled to room temperature. The resulting brown-black product was dialyzed against DI water (exchanged every 3 h for 24 h) and subsequently freeze-dried at −60 °C for 48 h to yield purified N-CQDs.

2.4. Synthesis of the rGO/N-CQD Composite. Three rGO/N-CQD composite samples were synthesized hydrothermally. GO powder was dispersed in 10 mL of DI water via sonication for 30 min. Subsequently, 1.0507 g $C_6H_8O_7$ and 335 μL $C_2H_8N_2$ were added to the GO suspension. The mixture was then heated in a 50 mL autoclave at 150 °C for 5 h. Finally, the resulting blackish-brown suspension was dialyzed using a 1000 Da membrane. The synthesis steps are outlined in Figure 1.

The suspension was dialyzed against DI water (exchanged every 3 h for 24 h) and then freeze-dried at −60 °C for 48 h. Three GO/N-CQD composites with varying compositions were synthesized according to Table 2. The rGO nanosheets, chosen for their high TC, formed the primary component of the composite. Quantum dots were incorporated to enhance the rGO stability and improve heat transfer across the plates; consequently, rGO percentages below 50% were not evaluated. The optimal composite ratio was selected based on TC and stability measurements. Transmission electron microscopy (TEM) images and other data confirmed that further ratio optimization was unnecessary as the chosen formulation showed stable dispersion and favorable structural features.

2.5. Characterization and Equipment. The optical properties of GO, N-CQD, and rGO/N-CQDs were determined by using a UNICO 2800 model UV−vis spectrometer. A functional group analysis was performed using FTIR spectroscopy with a Nicolet 370 spectrometer. The Raman spectrum of various nanomaterials was obtained using an Almega Thermo Nicolet Raman spectrometer with 532 nm laser excitation. X-ray diffraction was performed using Bruker D8-Advanced XRD equipment over a broad range of angles (2θ = 5 to 80°) with monochromatized Cu Kα radiation (λ = 15406 Å). The

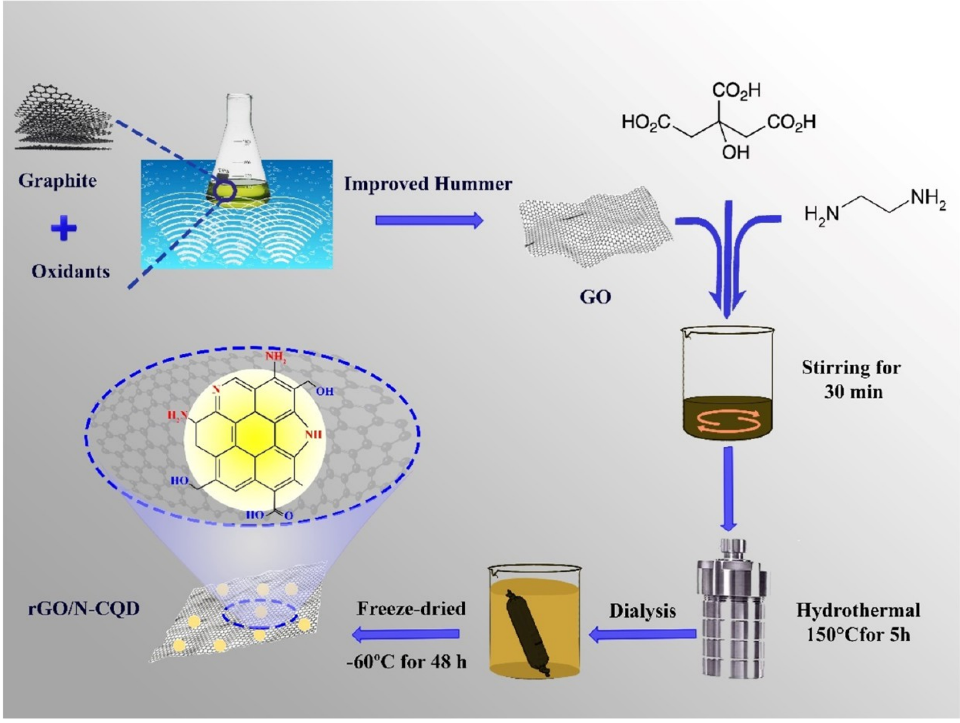

Figure 1. Schematic illustration of the synthesis process of the rGO/N-CQD composite.

Table 2. Amounts of Nanomaterials and DI Water for Nanocomposite Synthesis

sample	N-CQD (g)	GO (g)	DI water (mL)
rGO/N-CQD$_{50/50}$	0.016	0.016	10
rGO/N-CQD$_{60/40}$	0.016	0.024	10
rGO/N-CQD$_{70/30}$	0.016	0.037	10

transmission electron microscopy (TEM) characterization was performed by a Zeiss EM10, Germany, 80 kV. X-ray photoelectron spectroscopy (XPS) measurements were performed by using a Bes-Tec (Germany) electron spectrometer with monochromatic Mg Kα radiation (1253.6 eV). Atomic force microscopy (AFM) images were obtained by using an atomic force microscope from ARA Pajoohesh (ARA Pajoohesh Inc., Tehran, Iran). Energy Dispersive X-ray (EDX) microanalysis and elemental mapping were recorded using Tescan-Vega2, XMU. The Zeta potential of nanofluids was measured using a zeta potential meter (Zeta Compact, CAD Instruments, France). The TC of nanofluids was determined using a KD2 Pro analyzer (Decagon Devices, Inc., USA). The specific heat capacities (C_p) samples were measured from 20 to 80 °C with a temperature rise rate of 5 °C/min using a differential scanning calorimeter (Swiss Mettler-Toledo-DSC3). The thermal images were visualized using an infrared (IR) Camera (DT-980, China).

2.6. Preparation of N-Doped CQD, GO, and rGO/N-CQD-Based Nanofluids. GO, N-CQD, and rGO/N-CQD nanofluids were prepared in DI water via a two-step method at concentrations of 0.0060, 0.0125, 0.0250, and 0.0500%w. No dispersants were used, and the resulting samples were sonicated for 30 min.

2.7. Thermophysical Characteristics. The TC of the nanofluid, its primary thermophysical property, was measured using the transient hot wire method with a KD2 Pro thermal property analyzer.[30] Nanofluids were prepared at 0.0500%w concentration and sonicated for 30 min before vertical insertion of the KS-1 single sensor. The TC of GO, N-CQD, and rGO/N-CQDs was measured at 40 °C with 5% accuracy. Thermal conductivity ratio (TCR) and thermal conductivity enhancement (TCE) were calculated using eqs 1 and 2, where k_{nf} and k_{bf} are the thermal conductivity coefficients of the nanofluid and base fluid, respectively.[31]

$$\mathrm{TCR} = \frac{K_{nf}}{K_{bf}} \tag{1}$$

$$\%\mathrm{TCE} = \frac{K_{nf} - K_{bf}}{K_{bf}} \times 100 \tag{2}$$

The C_p is a thermal property directly linked to heat storage and transfer in energy systems.[32] Therefore, the C_p of the base fluid and nanofluids was measured by using a differential scanning calorimeter.

2.8. Development of ANN. Repetitive testing makes laboratory research time-consuming and expensive, leading researchers to explore more advanced computing methods. ANNs are favored for accurately predicting nanofluid thermophysical properties.[33] ANNs, similar to the human brain, learn relationships between inputs and outputs. This learning is affected by the number of layers and neurons, particularly those at the input and output of hidden layers.[34] Transfer functions are also crucial for interlayer communication and network structure. To find the optimal neural network structure, the following steps were taken:

- The number of hidden neurons was changed between 4 and 10
- The activation functions for the hidden layer and output layer were varied between Tan-Sig and Purelin
- In total 28 different structures were trained and the one with the lowest error was chosen

In this study, it was found that the Tan-Sig for the hidden layer and Purelin for the output layer is the best structure, Tan-Sig function defined in eq 3.[35]

$$f(x) = \frac{2}{1 + \exp(-2x)} - 1 \tag{3}$$

The Levenberg–Marquardt method was selected for network training, and all input data were normalized according to eq 4.[35]

$$X_{norm} = 2 \times \frac{X - X_{min}}{X_{max} - X_{min}} - 1 \tag{4}$$

The prediction model's performance was assessed using common error metrics: percent error (δ), Root Mean Squared Error (RMSE), Relative Root Mean Squared Error (rRMSE), Mean Absolute

Table 3. Summary of the Statistical Metrics Utilized in the Study

metric	eq	description
δ	$\left\lvert \frac{X_A - X_E}{X_E} \right\rvert \times 100$	Percent error quantifies the difference between an estimated and an actual value as a percentage of the actual value. A smaller percent error signifies a more accurate estimate.[36]
RMSE	$\sqrt{\frac{1}{n}\sum_{i=1}^{n}(X_A - X_E)^2}$	RMSE offers insights into the short-term performance of prediction models. Its value is always positive, and a value close to zero is desired.[37]
rRMSE	$\frac{\sqrt{\frac{1}{n}\sum_{i=1}^{n}(X_A - X_E)^2}}{\overline{X}_E} \times 100$	rRMSE is calculated using the RMSE and the average value of the measured data. A smaller rRMSE value indicates better performance of the prediction model.[38] The success of the prediction model is categorized as follows: - Excellent: rRMSE < 10% - Good: 10% < rRMSE < 20% - Fair: rRMSE < 30%
MAPE	$\frac{1}{n}\sum_{i=1}^{n}\left\lvert \frac{X_E - X_A}{X_E} \right\rvert \times 100$	MAPE measures the accuracy of a prediction model by comparing the average of the absolute values of prediction errors to the absolute values of actual data. A lower MAPE value indicates better model performance.[37] The classification of prediction accuracy is as follows: - High prediction accuracy: MAPE ≤ 10% - Good prediction: 10% < MAPE ≤ 20% - Reasonable prediction: 20% < MAPE ≤ 50% - Inaccurate prediction: MAPE > 50%
R^2	$1 - \frac{\sum(X_E - X_A)^2}{(X_E - \overline{X}_E)^2}$	This method indicates how effectively a model can predict a given set of measured data. The value ranges from 0 to 1, with an R^2 value closer to 1 representing better performance.[39]

Percentage Error (MAPE), and the Coefficient of Determination (R^2) (Table 3). These metrics compare the ANN-predicted TC values (X_A) to the experimental TC values (X_E), with $\overline{X}_i$ representing the mean of the experimental values and n denoting the number of measurements. Based on the analysis of varying neuron numbers in the hidden layer, a configuration with 6 neurons was selected (Figure 2).

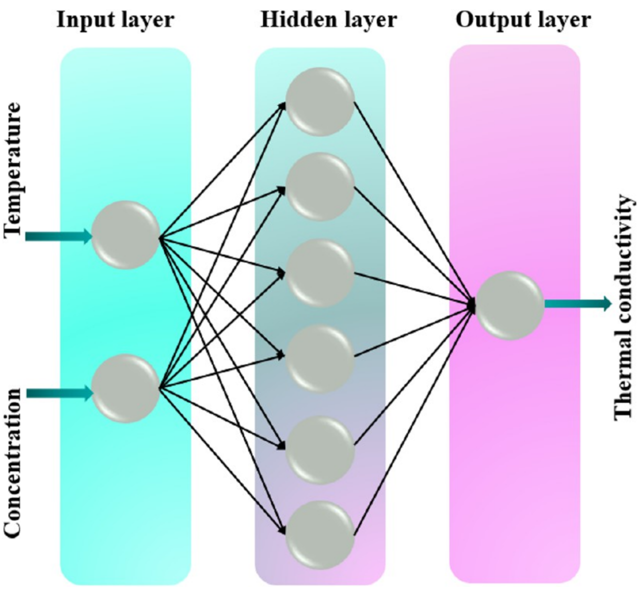

Figure 2. Optimal ANN configuration.

2.9. Stability Analysis of Nanofluids. Common stability evaluation methods for nanofluids include sedimentation, centrifugation, zeta potential, and spectral absorbency analysis. Sedimentation, the simplest method, infers stability from the weight or volume of nanoparticle sediment under an external force. Visual observation via sedimentation photographs is also frequently used. Spectral absorbency analysis, which leverages the linear relationship between absorbency intensity and nanoparticle concentration, provides a quantitative measure of nanofluid concentration, making it advantageous over other techniques.[40] Zeta potential, the electric potential at the slipping plane of the interfacial double layer, correlates with the stability of colloidal dispersions.[41] In this work, nanofluid stability was assessed through zeta potential analysis and absorption spectra measurements. UV−vis spectroscopy, performed within the 200−900 nm range, analyzed the relationship between light absorption and the wavelength. The absorbance of 0.0500%w rGO/N-CQD nanofluids was measured in the upper part of the sample at 3-day intervals after sonication.

2.10. Measuring the Optical Properties of Nanofluids. Nanofluid optical properties are crucial for photothermal applications. UV−vis−NIR transmission spectra of the base fluid and nanofluids were measured using a spectrophotometer from 300 to 1000 nm with ±1 nm accuracy. Extinction coefficients ($\alpha(\lambda)$) were then calculated from transmittance ($T(\lambda)$) data based on the Beer−Lambert law using eq 5 to characterize the nanofluids' optical behavior.[42]

$$\alpha(\lambda) = \frac{-1}{L}T(\lambda) \tag{5}$$

Among the law, l is the optical length of a quartz cuvette, i.e, 10 mm. To better understand the heat transfer properties of the fluid in the solar collector, the theoretical absorption of the spectral intensity and its amount for the base fluid and nanofluids were calculated using eq 6.[43,44] In this eq, $I_A(\lambda)$ represents the solar radiation absorbed by the nanofluid. $I_{AM1.5}(\lambda)$ represents the standard solar power spectrum, as defined by ASTM G173-03.

$$I_A(\lambda) = I_{AM1.5}(\lambda)[1 - T(\lambda)] \tag{6}$$

In solar energy absorption, the solar-weighted absorption fraction (A_m) represents the percentage of solar energy absorbed by the nanofluids, as defined by eq 7, where x is the penetration distance.[14]

$$A_m = \frac{\int_{\lambda_{min}}^{\lambda_{max}} I_{AM1.5}(\lambda)[1 - e^{-\alpha(\lambda)x}]d\lambda}{\int_{\lambda_{min}}^{\lambda_{max}} I_{AM1.5}(\lambda)d\lambda} \tag{7}$$

In DASCs, a thin working fluid layer absorbs the solar radiation. High surface temperatures and radiation losses can cause environmental heat loss. Inadequate collector height hinders nanofluid absorption, significantly reducing the solar energy conversion efficiency. Thus, optimizing A_m is crucial for DASC efficiency. The average nanofluid absorption can be calculated using eq 8.[45]

$$A_{NF} = \frac{\int_{\lambda_{min}}^{\lambda_{max}} I_{NF}(\lambda)d\lambda}{\int_{\lambda_{min}}^{\lambda_{max}} I_{AM1.5}(\lambda)d\lambda} \tag{8}$$

2.11. Experiments on Solar Thermal Conversion. A simple experimental setup (Figure 3) was used to measure the photothermal conversion efficiency of the nanofluid. This setup included a 100 mL

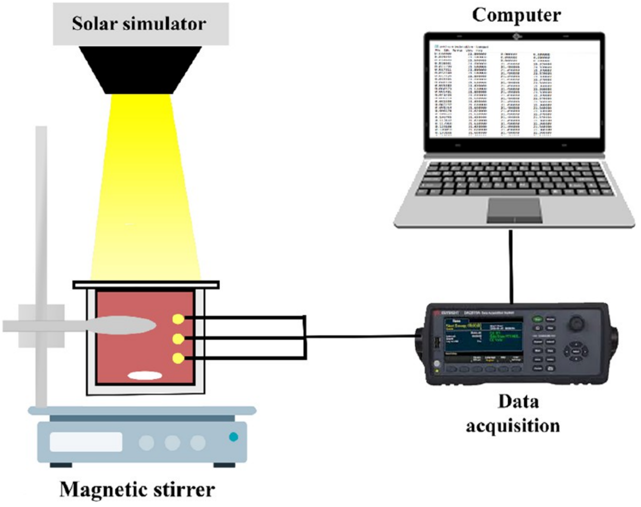

Figure 3. Schematic of the photothermal conversion experimental setup.

polypropylene beaker (5 cm inner diameter and 7 cm height; Figure S1) stirred at ∼400 rpm to ensure uniform thermal distribution. The beaker was suspended to prevent contact with the magnetic stirrer, insulated with low thermal conductivity foam, and covered with a quartz plate to minimize heat loss and evaporation. This closed, insulated system with low operating temperatures minimized evaporation and heat loss in solar thermal conversion experiments.[46] Three T-type thermocouples, positioned at 20, 30, and 40 mm from the beaker bottom, monitored temperature during 60 min irradiation with simulated sunlight (Arvin Nano Equipment, Iran) at intensities of 1, 2, and 3 suns (1 sun = 1000 W/m^2), recording data every 1 s. While symmetrical thermocouple placement improves spatial averaging, 400 rpm stirring ensured radial uniformity of temperature, and the vertical profile prioritized detecting axial stratification, critical for photothermal efficiency calculations. The total energy absorbed by the nanofluids (Q_A) was calculated using eq 9 to determine their photothermal conversion performance.[47]

$$Q_A = \sum_{1}^{z} C_P \sum_{1}^{i} (m_i dT_i) \tag{9}$$

In this equation, C_p is the working fluid's specific heat capacity, and ΔT_i and mi represent the nanofluid's temperature increase and mass during a specific irradiation time. The η was then calculated using eq 10, where I is solar radiation intensity, A is the nanofluid's irradiated surface area, and t is the irradiation time.[48]

$$\eta = \frac{Q_A}{\int_0^t IA dt} \tag{10}$$

Measurement errors in nanofluid mass (m), thermocouple temperature (T), and radiation intensity (I) contribute to the overall error in the photothermal conversion experiment. Consequently, the relative error (E_R) of the photothermal conversion efficiency can be determined using eq 11.[49]

$$E_R = \sqrt{\left(\frac{\delta I}{|I_i|}\right)^2 + \left(\frac{\delta T_1}{|T_1|}\right)^2 + \left(\frac{\delta T_2}{|T_2|}\right)^2 + \left(\frac{\delta T_3}{|T_3|}\right)^2 + \left(\frac{\delta m_i}{|m_i|}\right)^2} \tag{11}$$

The experimental results are reliable as the photothermal conversion experiments have a maximum uncertainty of only 1.4%.

3. RESULTS AND DISCUSSION

3.1. Structure and Morphology. UV−vis absorption of the nanomaterials was measured using a spectrophotometer

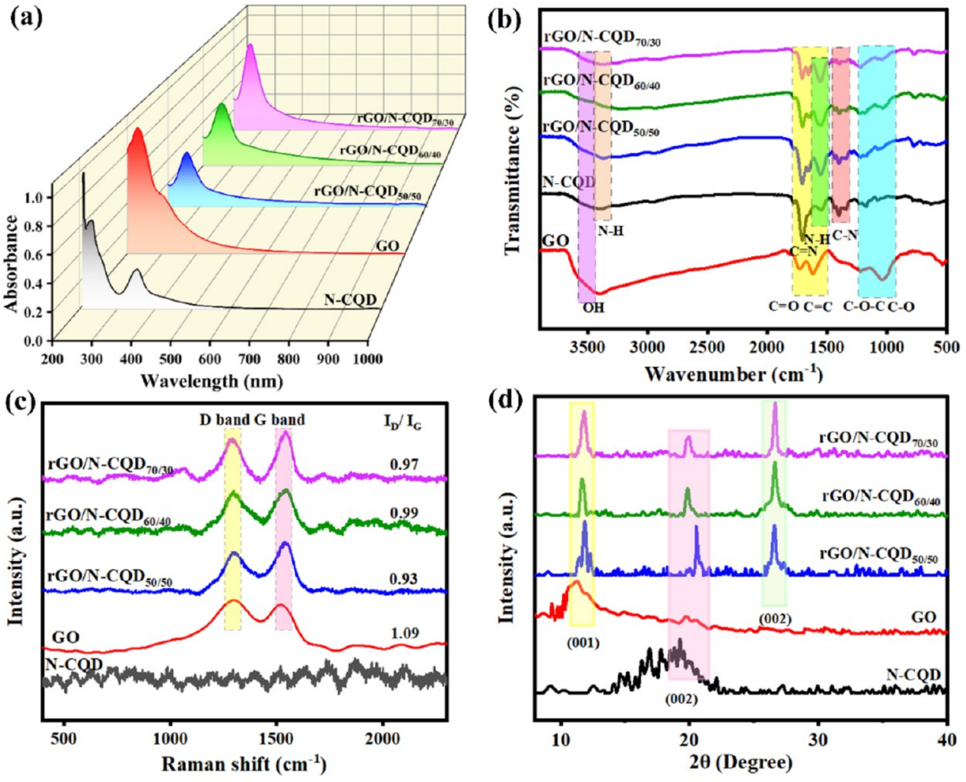

Figure 4. (a) UV−visible absorption spectra of N-CQD, GO, rGO/N-CQD$_{50/50}$, rGO/N-CQD$_{60/40}$, and rGO/N-CQD$_{70/30}$ samples, (b) FTIR spectrum of GO, N-CQD, rGO/N-CQD50/50, rGO/N-CQD$_{60/40}$, and rGO/N-CQD$_{70/30}$ samples, (c) Raman spectra, and (d) XRD patterns of N-CQD, GO, rGO/N-CQD$_{50/50}$, rGO/N-CQD$_{60/40}$, and rGO/N-CQD$_{70/30}$ samples.

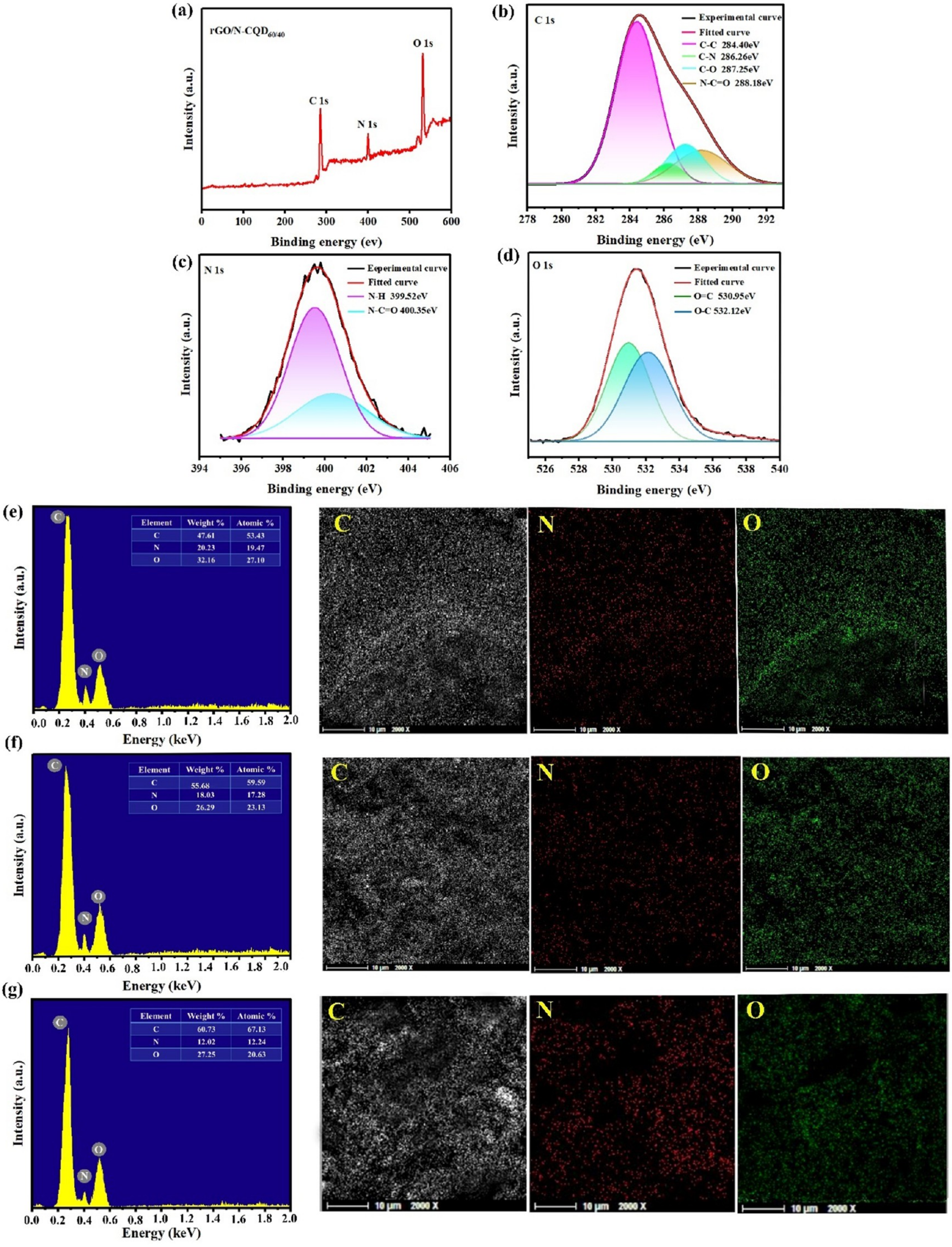

(e)

Element	Weight %	Atomic %
C	47.61	53.43
N	20.23	19.47
O	32.16	27.10

(f)

Element	Weight %	Atomic %
C	55.68	59.59
N	18.03	17.28
O	26.29	23.13

(g)

Element	Weight %	Atomic %
C	60.73	67.13
N	12.02	12.24
O	27.25	20.63

Figure 5. XPS spectra of the rGO/N-CQD$_{60/40}$ composite: (a) survey scan, (b) C 1s, (c) N 1s, and (d) O 1s, and the EDAX spectra and elemental mapping of (e) rGO/N-CQD$_{50/50}$, (f) rGO/N-CQD$_{60/40}$, and (g) rGO/N-CQD$_{70/30}$.

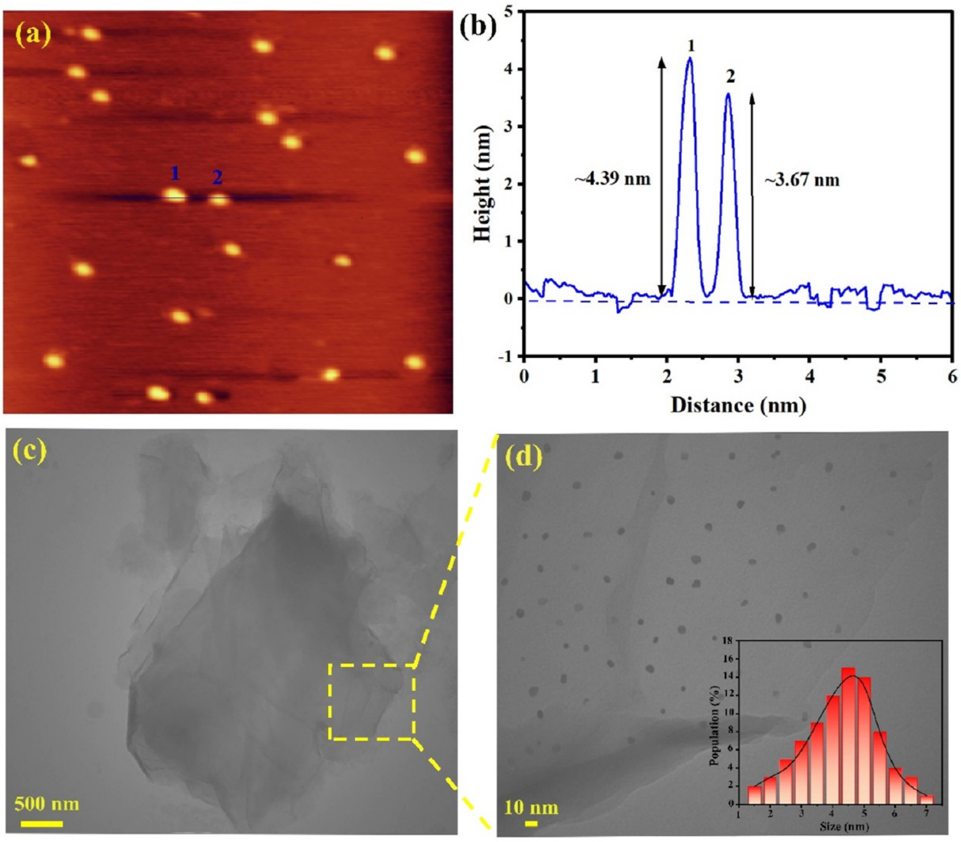

Figure 6. (a) AFM image of N-CQD, (b) the corresponding height profile along the line in (a), (c), and (d) TEM image of the rGO/N-CQD$_{60/40}$ composite.

with DI water as the reference. Figure 4a shows that GO nanosheets exhibit maximum absorption at 230 and 260 nm, corresponding to π−π* and n−π* transitions, respectively. These transitions are attributed to C=C (sp^2 hybridization) and C=O bonds associated with oxygen groups.[50] N-CQDs displayed maximum absorption at 231 and 353 nm, also related to π−π* and n−π* transitions. The high absorbance at these wavelengths is attributed to C=C and C=O bonds on the quantum dot surface, respectively.[51] In rGO/N-CQD composites (50/50, 60/40, and 70/30), the maximum absorption peak initially at 230 nm in GO shifted to higher wavelengths of 257, 262, and 258 nm, respectively. This red shift of the π−π* transition indicates the reduction of GO to rGO during the composite's hydrothermal preparation.[52]

FTIR analysis (Figure 4b) confirmed the presence of functional groups in the prepared nanostructures. The GO spectrum exhibited characteristic peaks at 3405.67 cm^{-1} (O−H stretching), 1727.91 cm^{-1} (C=O stretching), and 1031.73 cm^{-1} (C−O stretching), indicating the disruption of graphite's π bonds and the introduction of oxygen-containing groups during GO synthesis. The peak at 1619.91 cm^{-1} suggests the presence of residual sp^2 groups.[53] Spectra of N-CQD and rGO/N-CQD composites showed O−H and N−H stretching vibrations in the 3296−3396 cm^{-1} range and a small peak at ∼1295 cm^{-1}, attributed to C−H stretching and sp^3 hybridized carbon. C=O stretching vibrations were observed at ∼1712 cm^{-1}. A high-intensity absorption peak in the CQD spectrum (1565−1658 cm^{-1}) was assigned to C=C and C=N stretching vibrations.[54] N−H bending vibrations appeared at 1550−1556 cm^{-1} in quantum dots and rGO/N-CQD composites. Finally, C−O and C−O−C bending vibrations were detected at 1382−1384 cm^{-1} and 1240 cm^{-1} in N-CQD and rGO/N-CQD composite samples. In summary, FTIR effectively characterized the structures and surface functional groups of GO, N-CQD, and the rGO/N-CQD composites. FTIR analysis confirms the formation of the rGO/N-CQD composite, as spectral shifts were observed in the composite compared to pure rGO.

Raman spectroscopy (100−4000 cm^{-1}, Figure 4c) was employed to analyze the vibrational states of GO, N-CQD, rGO/N-CQD$_{50/50}$, rGO/N-CQD$_{60/40}$, and rGO/N-CQD$_{70/30}$. The GO spectrum exhibited D and G bands at 1341 and 1563 cm^{-1}, respectively. The D band, indicative of defects and disorder in the graphene lattice (A_{1g} vibration mode of sp^2 carbon) due to oxidation, correlates with increased C−C bonds and decreased sp^2 in-plane vibrations. The G band corresponds to graphite lattice vibrations with E_{2g} symmetry.[55] The I_D/I_G ratio, a measure of graphene sheet oxidation, was 1.09 for GO. For N-CQD, D and G bands are typically found at 1348 and 1547 cm^{-1};[56] however, in this study, the strong fluorescence of N-CQD, even with 785 nm excitation, prevented observation of these bands.[57] The rGO/N-CQD composites exhibited D and G bands at 1299 and 1541 cm^{-1} (rGO/N-CQD$_{50/50}$), 1296 and 1543 cm^{-1} (rGO/N-CQD$_{60/40}$), and 1295 and 1541 cm^{-1} (rGO/N-CQD$_{70/30}$). The corresponding I_D/I_G ratios were 0.93, 0.99, and 0.97, respectively. The lower I_D/I_G ratio in rGO/N-CQD composites (0.93−0.99) compared to GO (1.09) indicates GO reduction and the restoration of sp^2-hybridized carbon domains, resulting in more ordered graphitic structures. This

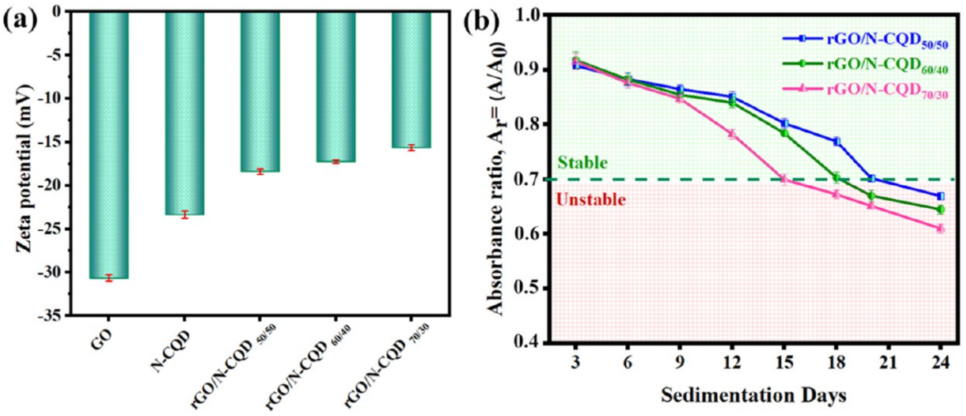

Figure 7. (a) Zeta potential of GO, N-CQD, rGO/N-CQD $_{50/50}$, rGO/N-CQD$_{60/40}$, and rGO/N-CQD$_{70/30}$ nanofluids. (b) Absorbance ratio of rGO/N-CQD nanofluids over 24 days.

enhanced order is crucial for improving electrical conductivity,[58] which, in turn, can increase the TC of graphene nanosheets, beneficial for photothermal applications.

XRD analysis (Figure 4d) revealed the crystal structure of the nanostructures. GO and N-CQD powders exhibited characteristic peaks at $2\theta = 11.20°$ (001 plane)[59] and 19.24° (002 plane),[60] respectively. Hydrothermally synthesized rGO/N-CQD composites (50/50, 60/40, and 70/30) showed three peaks at $2\theta = 11.85$, 20.52, and 26.58; 11.65, 19.83, and 26.59; and 11.81, 19.97, and 26.64°, respectively. These peaks correspond to graphene nanosheets (001 plane), N-CQD (002 plane), and rGO (002 plane),[61] indicating a successful reduction of GO to rGO during the hydrothermal process. The coexistence of graphene and rGO peaks suggests partial GO reduction.

XPS analysis was utilized to determine the surface's chemical composition and identify the type of bond present (Figure 5a). Examination of the XPS spectrum of the rGO/N-CQD$_{60/40}$ composite revealed three characteristic peaks for C 1s, N 1s, and O 1s at 285, 400, and 531.4 eV, respectively. The C 1s peak was split into four peaks at 284.40, 286.26, 287.25, and 288.18 electron volts, which are associated with C−C, C−N, C−O, and N−C═O bonds, respectively (Figure 5b). The N 1s peak was divided into two peaks at 399.52 and 400.35 eV, indicating the presence of N−H and N−C═O bonds, respectively (Figure 5c). The separated peaks of O 1s show two peaks at 530.95 and 532.12 electron volts, corresponding to O═C and O−C bonds, respectively (Figure 5d).[62,63] EDAX was used for semiquantitative elemental analysis of carbon materials.[64] The rGO/N-CQD samples were drop-cast onto carbon tape and vacuum-dried for uniform dispersion. Figure 5e−g shows the EDAX spectra and elemental maps of rGO/N-CQD composites. N-CQD incorporation on rGO nanosheets was quantified by the N/C atomic ratio, which was 0.364, 0.289, and 0.182 for rGO/N-CQD$_{50/50}$, rGO/N-CQD$_{60/40}$, and rGO/N-CQD$_{70/30}$, respectively.

AFM provides unique morphological insights that complement SEM/TEM, particularly for nanoparticle height, surface roughness, and mechanical properties.[65] AFM (Figure 6a) revealed the morphology of the hydrothermally synthesized N-CQDs. Height profiling (Figure 6b) between two adjacent N-CQDs indicated a size of approximately 4 nm. TEM imaging (Figure 6c) of the rGO/N-CQD$_{60/40}$ composite confirmed the successful anchoring of N-CQDs onto rGO nanosheets (Figure 6d), with an average N-CQD diameter of 4−5 nm (Figure 6d). TEM confirms that the rGO is attached to the N-CQD, unlike the random clustering anticipated in a simple binary mixture. If N-CQDs were only mixed (as a binary nanofluid), they would appear as random clusters surrounding the rGO. The close agreement (4−5 nm) between AFM height and TEM lateral diameter indicates minimal particle aggregation or stacking, validating the AFM-derived N-CQD thickness.

3.2. Stability Characterization.

Nanofluid suspension stability is commonly improved by adding surfactants or chemically functionalizing nanoparticle surfaces.[66] While surfactants are limited by irreversible high-temperature degradation that weakens their bond with nanoparticles, functionalized nanoparticles show promise for achieving long-term, high-temperature stability.[67] Surface modification chemically binds functional groups, enhancing compatibility with the host environment.[68] For example, N-CQD was used to compensate for the loss of hydrophilic oxygen groups on GO nanosheets during hydrothermal synthesis, leveraging the numerous hydroxyl, carbonyl, and amino groups on the N-CQD surface to enhance the solubility and stability. Zeta potential and absorption spectrum analyses were used to investigate the stability of various nanofluids prepared from composites. Zeta potential measurements, crucial for understanding electrostatic interactions between nanomaterials, were performed at 25 °C and pH 6.24 for GO, N-CQD, rGO/N-CQD$_{50/50}$, rGO/N-CQD$_{60/40}$, and rGO/N-CQD$_{70/30}$ nanofluids. The respective zeta potential values were −30.65, −23.35, −18.4, −17.24, and −15.66 mV (Figure 7a). UV−vis spectroscopy (200−800 nm) assessed the wavelength-dependent light absorption of 0.0500%w nanocomposite-based nanofluids. Figure 7b illustrates the normalized absorption intensity (A/A_0) over 24 days, where A and A_0 are the maximum absorption intensities at a given day and preparation time, respectively, within the 200−800 nm range. The rGO/N-CQD$_{50/50}$, rGO/N-CQD$_{60/40}$, and rGO/N-CQD$_{70/30}$ nanofluids (0.0500%w) exhibited good dispersion and stability up to 20, 18, and 15 days, respectively. Sedimentation began gradually after these periods, with absorption intensity decreasing to 0.7 of the initial values.[69] Nanofluids' stability was observed for at least 15 days (Figure S2). Although zeta potential values exceeding ±30 mV typically indicate stable dispersions,[70] these nanofluids, with moderate zeta potential measured at laboratory temperature and neutral pH, remained stable for 15−20 days, as confirmed by UV−vis absorption and

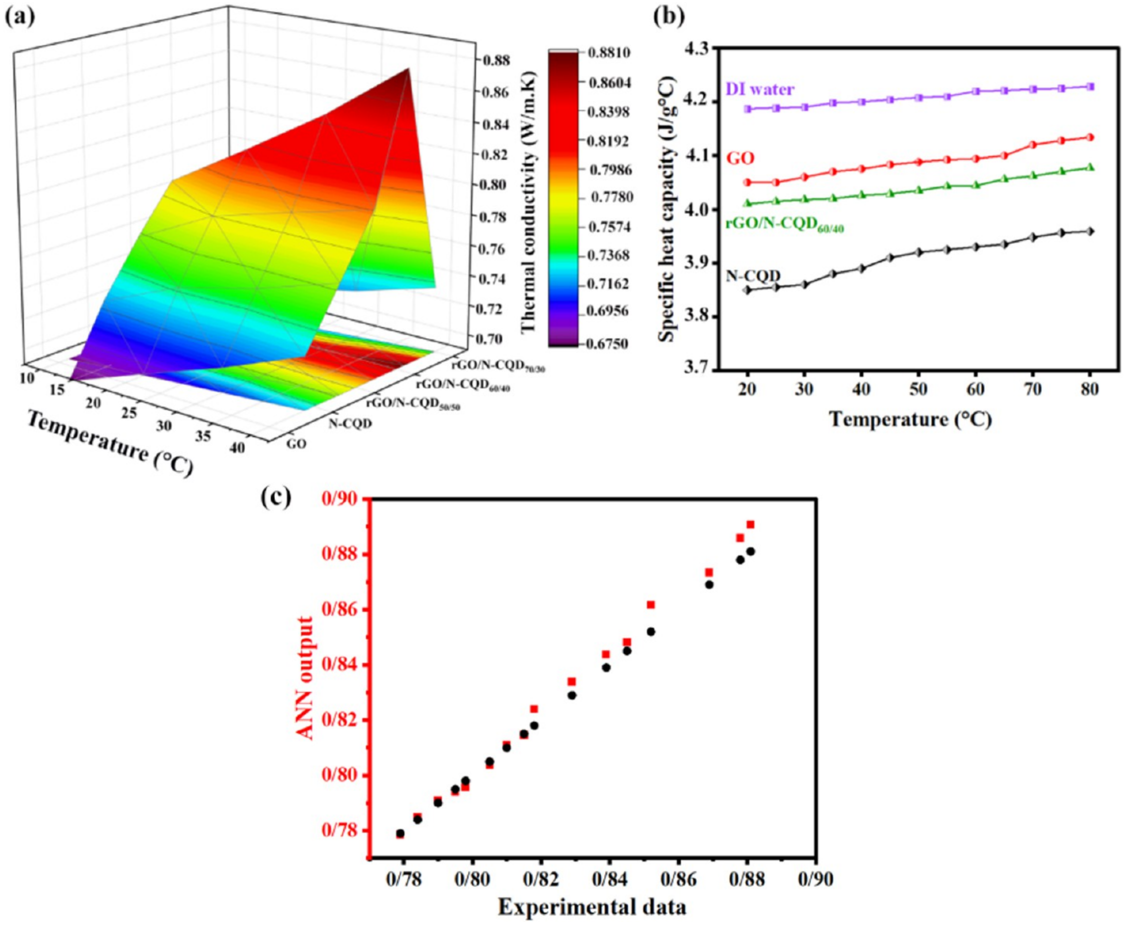

Figure 8. (a) TC of various nanofluids with temperature at 0.0500%w, (b) C_p of N-CQD, rGO/N-CQD$_{60/40}$, GO nanofluids, and DI water, and (c) comparison between TC of experimental data with ANN output for the rGO/N-CQD$_{60/40}$ nanofluid.

visual inspection. This stability is attributed to the enhanced electrostatic repulsion from the combination of rGO and nitrogen-doped quantum carbon. Furthermore, the dynamic conditions within the intended closed-loop system (DASCs) will likely further stabilize the nanofluid and prevent nanoparticle aggregation, contrasting with the static conditions during the zeta potential measurement.

3.3. Thermophysical Measurement. While nanocarbon structures inherently possess high TC, oxygen functional groups drastically reduce TC by 2−3 orders of magnitude due to disrupted lattice symmetry and induced local strain. GO nanosheets exhibit anisotropic TC, and vacancies in GO strips negatively impact TC. Furthermore, increased phonon scattering from GO defects further diminishes the TC.

To enhance the TC, GO nanosheets were coated with N-CQD, creating a composite material. The TC of five nanofluids (GO, N-CQD, rGO/N-CQD$_{50/50}$, rGO/N-CQD$_{60/40}$, and rGO/N-CQD$_{70/30}$) was measured at concentrations of 0.0060, 0.0125, 0.0250, and 0.0500%w between 10 and 40 °C using a KD2 sensor-equipped heat processor. All nanofluids exhibited the highest TC at 40 °C and 0.0500%w (Figure S3a−e). At 0.0500%w, the rGO/N-CQD$_{60/40}$ nanofluid displayed the highest TC compared to the other nanofluids (Figure 8a). TCR and TCE% values were calculated using eqs 1 and 2 and are presented in Figure S4a,b. The GO nanofluid yielded a TC of 0.724 W/m·K, with a TCR of 1.23 and a TCE % of 23.12%. The N-CQD nanofluid showed a TC of 0.761 W/m·K, with a TCR of 1.29 and a TCE % of 29.42%. The addition of N-CQD quantum dots increased the TC of the GO nanofluid. TC values for rGO/N-CQD$_{50/50}$, rGO/N-CQD$_{60/40}$, and rGO/N-CQD$_{70/30}$ were 0.799, 0.881, and 0.733 W/m·K, respectively, with corresponding TCR and TCE % values of 1.35, 35.88%; 1.49, 49.82%; and 1.24, 24.65%. The rGO/N-CQD$_{60/40}$ composite exhibited the highest TC increase compared to those of GO and N-CQD nanofluids. This excellent thermal conductivity is crucial for DASC applications as it minimizes heat loss by rapidly transferring energy from the surface layer to the fluid bulk.

Figure 8b shows the C_p values of the base fluid and nanofluids at various temperatures. Nanofluids exhibit a lower C_p than the base fluid, and the C_p of all fluids increases with temperature. Consequently, the C_p values for the base fluid and nanofluids were modeled as temperature-dependent functions (eqs 12−15) to calculate the photothermal conversion efficiency.

$$C_p\ (\text{DI water}) = 8 \times 10^{-4}T + 4.1705\ (R^2 = 0.9824) \tag{12}$$

$$C_p\ (\text{GO}) = 1.4 \times 10^{-3}T + 4.0182\ (R^2 = 0.9726) \tag{13}$$

$$C_p\ (\text{rGO/N-CQD}_{60/40}) = 1.9 \times 10^{-3}T + 3.9833\ (R^2 = 0.9737) \tag{14}$$

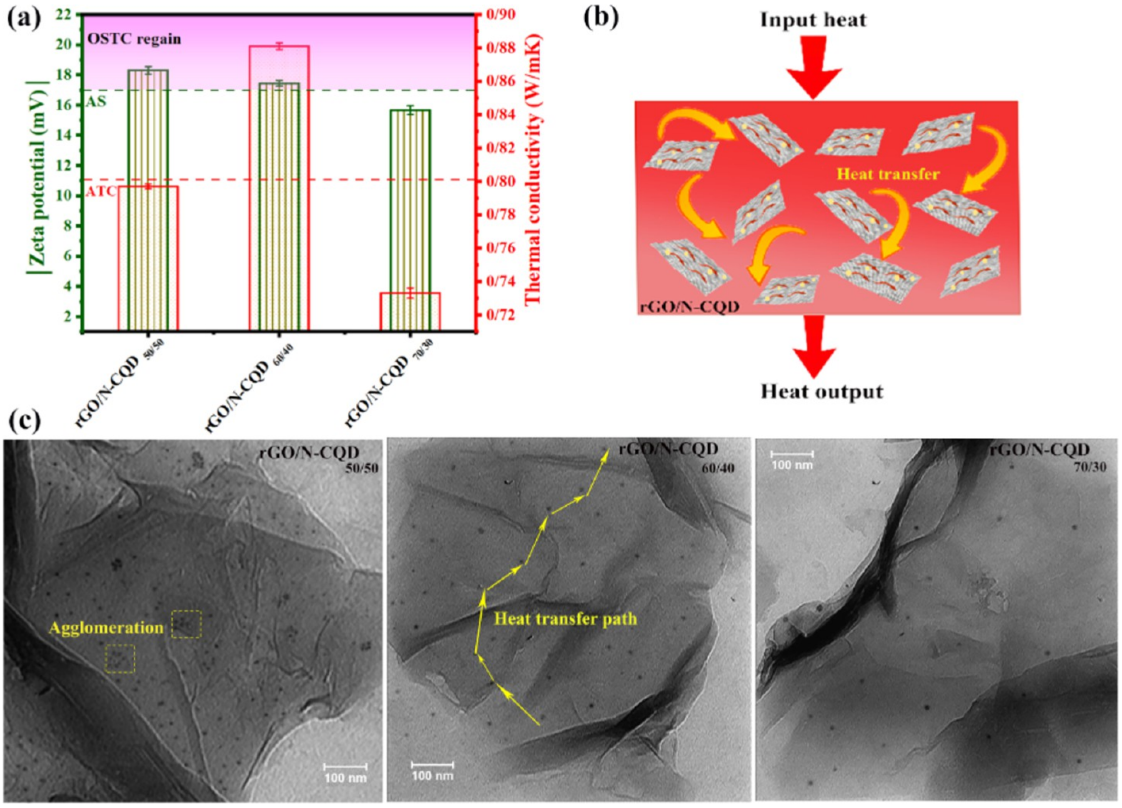

Figure 9. (a) TC and zeta potential of various nanofluids, (b) schematic of heat transfer in a nanofluid, and (c) TEM images of rGO/N-CQD$_{50/50}$, rGO/N-CQD$_{60/40}$, and rGO/N-CQD$_{70/30}$.

$$C_p\ (\text{N-CQD}) = 1.9 \times 10^{-3}T + 3.8118\ (R^2 = 0.9723) \tag{15}$$

C_P is the specific heat of the working fluid $(\mathrm{kJ\ kg^{-1}\ {}^{\circ}C^{1-}})$ and T is the temperature of the working fluid (°C) with R^2 as the coefficient of determination.

3.4. ANN Model. An ANN model with two input neurons, six hidden neurons, and one output neuron was developed to predict the TC of the rGO/N-CQD$_{60/40}$ nanofluid based on temperature and concentration. Experimental data and the ANN model's output are provided in Table S1, with a small δ indicating high accuracy. Figure 8C shows a strong agreement between the ANN-predicted and experimentally measured TC values. The temperature dependence of TC and corresponding δ at concentrations of 0.0060, 0.0125, 0.0250, and 0.0500%w is shown in Figure S5a−d. The small δ values further confirm the model's accuracy. The ANN model exhibited $R^2 = 0.9974$ and low rRMSE (training: 3.4843, testing: 6.5531), RMSE (training: 0.0348, testing: 0.0518), and MAPE (training: 4.0000, testing: 6.5531) values, demonstrating its effectiveness in predicting the TC of the rGO/N-CQD$_{60/40}$ nanofluid. The ANN analysis created a highly accurate predictive model for the TC of rGO/N-CQD60/40 nanofluids. With a high R^2 value and low error, the ANN effectively models the relationship among TC, temperature, and concentration. This validates experimental trends and allows for reliable extrapolation, enhancing the study's practical value for thermal applications.

3.5. Optimal Stability and Thermal Conductivity of the GO Nanofluid. Figure 8a shows that the rGO/N-CQD$_{60/40}$ nanofluid possesses the highest TC among the tested composites, while Figure 7a indicates that the rGO/N-CQD$_{50/50}$ nanofluid exhibits superior stability. For DASC applications, selecting a nanofluid with both high TC and stability is essential.[71] Figure 9a also presents the zeta potential and TC values for the three composite-based nanofluids. The nanofluid within the Optimal Stability and TC (OSTC) region, defined as above the average TC (ATC) and average stability (AS), was deemed to be optimal for light-to-heat conversion. These results demonstrate the influence of varying rGO and N-CQD percentages on the nanofluid TC and stability.

In DASCs, TC is crucial for evaluating the working fluid's heat transfer rate. Two-dimensional materials, with their high aspect ratio and surface area, reduce contact thermal resistance. Carbon quantum dots enhance heat transfer by directing it and increasing the surface area. As illustrated in Figure 9b, a higher TC enables faster heat transfer during photothermal conversion, minimizing heat loss. TC in rGO/N-CQD composites relies on phonon transport through continuous pathways, with N-CQDs acting as thermal bridges between rGO nanosheets to improve heat transfer. Morphological analysis (Figure 9c) shows varying N-CQD distributions and dispersion on rGO nanosheets. The rGO/N-CQD$_{50/50}$ composite's TEM image reveals N-CQD agglomeration, obstructing heat transfer. Conversely, rGO/N-CQD$_{60/40}$ exhibits a proportional N-CQD distribution, forming effective heat transfer pathways. However, rGO/N-CQD$_{70/30}$ lacks sufficient N-CQD for establishing such pathways. A 60/40 ratio of rGO to N-CQD (rGO/N-CQD$_{60/40}$) offers optimal dispersion, reducing interfacial resistance, and promoting the formation of efficient percolation networks. Conversely, agglomeration (50/50) or insufficient N-CQD density (70/30) disrupts these pathways. This behavior is consistent with

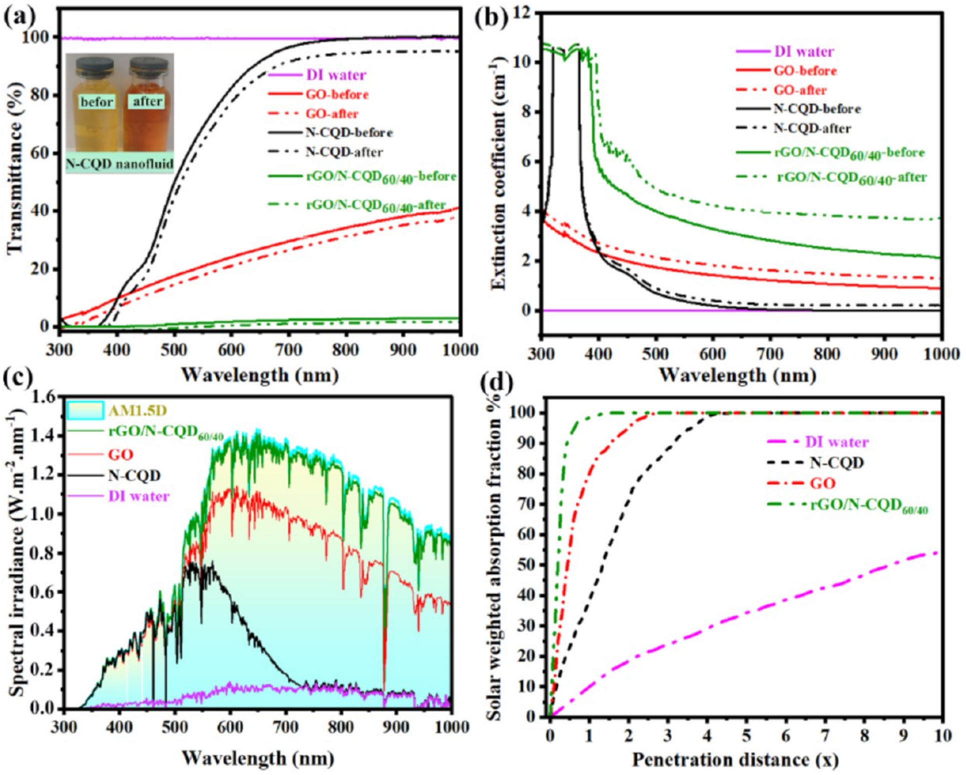

Figure 10. (a) transmission spectra, (b) extinction coefficient, (c) spectral solar irradiance of GO, N-CQD, rGO/N-CQD$_{60/40}$ nanofluids, and DI water, and (d) solar-weighted absorption fraction of different nanofluids and DI water.

Table 4. Comparison of Photothermal Conversions of Similar Materials

nanoparticle	base fluid	concentration	penetration depth	photothermal conversion efficiency (%)	ref
graphene	urea/choline chloride	40 ppm	1 cm	94.3	73
single-layer graphene	DI water	100 ppm	<2 cm	38.93	74
SiC-MWCNTs	ethylene glycol-	1%w	1 cm	97.3	49
GO	DI water	0.05%w	1 cm	72.5	7
rGO/N-CQD	DI water	0.05%w	1 cm	82.64	this work

percolation theory and effective medium principles, emphasizing the critical role of filler distribution in achieving high thermal conductivity. Percolation is the phenomenon where highly conductive particles, randomly distributed in a matrix, form a continuous chain connecting opposing faces.[72]

3.6. Optical Properties of Nanofluids. The optical properties of the base fluid and nanofluids are presented in Figure 10, emphasizing the importance of the absorption performance of the working fluid in DASC applications. Due to the dispersion of nanocarbon structures into the base fluid, nanofluids have lower transmittance in the visible light region compared to the base fluid. As shown in Figure 10a, the rGO/N-CQD$_{60/40}$ nanofluid exhibits significantly lower transmittance than GO and N-CQD alone, indicating that the hydrothermal composite enhances optical absorption. Exposure to solar radiation further decreases transmittance, correlating with color deepening (Figure 10a inset for the N-CQD nanofluid). These results suggest the potential of nanofluids as working fluids for DASCs.

Figure 10b shows that GO, N-CQD, and rGO/N-CQD nanofluids exhibit higher extinction coefficients than DI water in the visible range, indicating improved optical absorption due to the addition of nanocarbon structures. Notably, rGO/N-CQD$_{60/40}$ significantly enhances these properties, increasing the extinction coefficient from 0 in the base fluid to 4.9 cm^{-1}. Solar irradiation further increases the extinction coefficient of all nanofluids, making rGO/N-CQD$_{60/40}$ an excellent candidate for DASCs due to its exceptional optical characteristics. Figures 10c and S6 demonstrate the practical application potential of rGO/N-CQD$_{60/40}$, revealing its ability to access a significant portion of solar radiation energy, as indicated by its absorbed solar spectral irradiance curve's similarity to the standard solar spectrum and its maximum average absorptivity. Figure 10d presents the A_m of various nanofluids, showing that to harvest 99.95% solar energy at a 0.0500%w concentration, penetration depths of 4.6, 2.9, and 1.5 cm are required for N-CQD, GO, and rGO/N-CQD$_{60/40}$, respectively. Table 4 compares the photothermal conversion characteristics of the rGO/N-CQD$_{60/40}$ nanofluid with those of similar nanofluids.

3.7. Photothermal Performance of Nanofluids. Accurate determination of nanofluid photothermal efficiency requires a uniform temperature distribution. Solar radiation induces temperature increases, complicating energy calculations based on limited data points (Figure 11a). Thorough mixing achieved temperature uniformity, eliminating surface-to-bulk temperature differences (Figure 11b). Infrared images highlight the temperature distribution after 3600 s of solar irradiation, contrasting unstirred (Figure 11c) and stirred

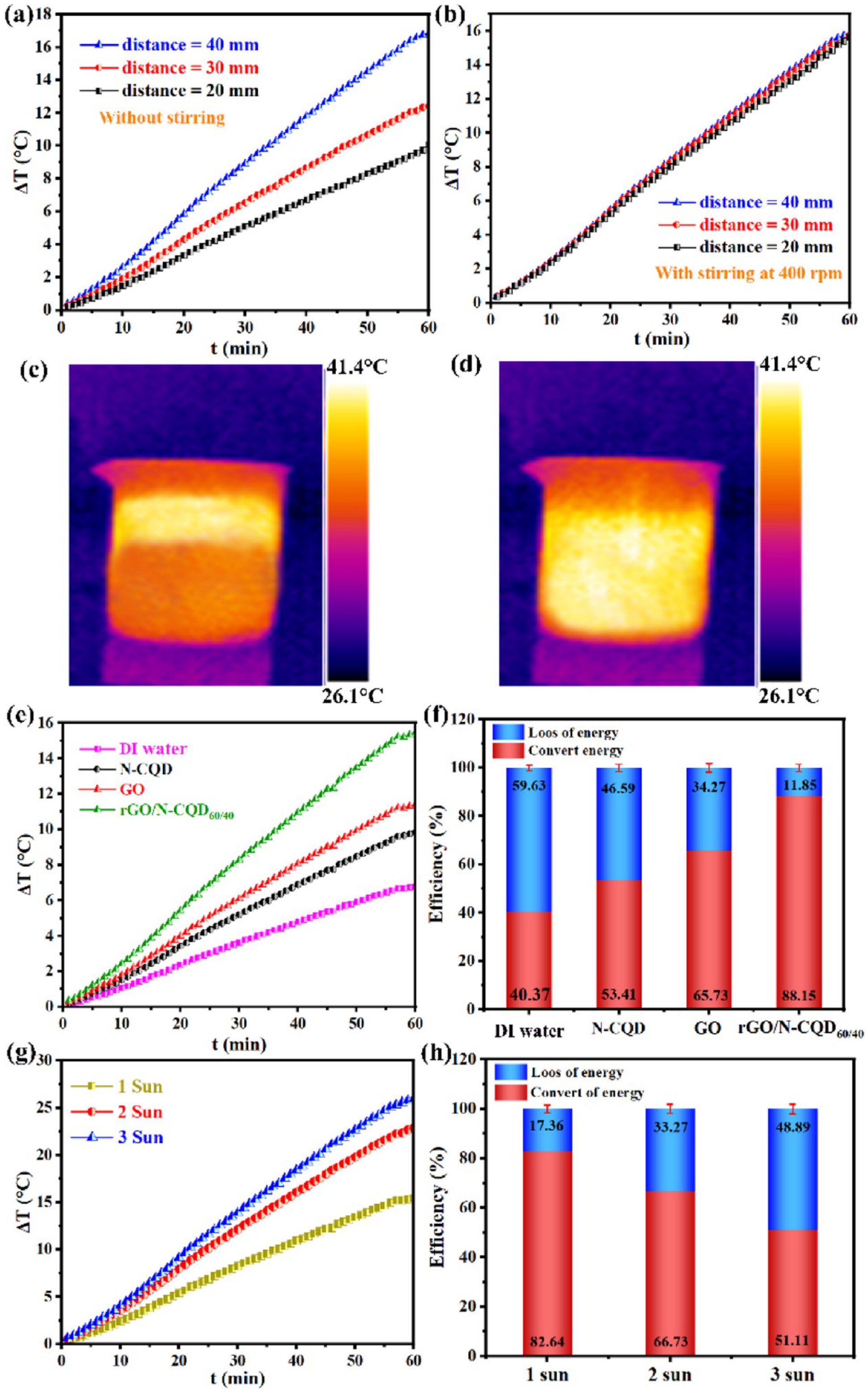

Figure 11. Temperature variation curves of the rGO/N-CQD$_{60/40}$ nanofluid under 1 Sun irradiation (a) without 400 rpm stirring, (b) with 400 rpm stirring, (c) infrared thermographs of rGO/N-CQD$_{60/40}$ without 400 rpm stirring, (d) with 400 rpm stirring, (e) temperature variation curves of nanofluids and DI water, (f) η of nanofluids and DI water, (g) temperature variation curves of rGO/N-CQD$_{60/40}$ nanofluid under different Sun irradiation, and (h) η of rGO/N-CQD$_{60/40}$ nanofluid under different Sun irradiation.

states (Figure 11d), facilitating subsequent calculations. After 3600 s of irradiation (Figure 11e), DI water, GO, N-CQD, and rGO/N-CQD$_{60/40}$ nanofluids reached maximum temperatures of 6.8, 11.4, 9.85, and 15.47 °C, respectively. Infrared thermographs (Figure S7a−d) corroborate these temperature differences, indicating that the rGO/N-CQD$_{60/40}$ nanofluid exhibited the greatest temperature increase. Key technical parameters for DT-980 used in this study are listed in Table S2. Figure S8 illustrates the energy absorbed by DI water, GO, N-CQD, and rGO/N-CQD$_{60/40}$ nanofluids. Under 1 Sun

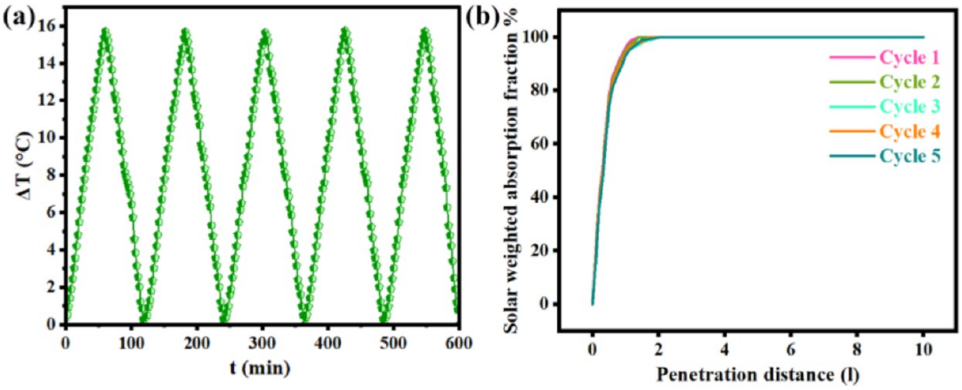

Figure 12. (a) Cycling performance of rGO/N-CQD$_{60/40}$ nanofluid at 1 Sun irradiation and (b) solar-weighted absorption fractions of the rGO/N-CQD$_{60/40}$ nanofluid after each heating−cooling cycle.

irradiation, rGO/N-CQD60/40 absorbed the most energy (5840.55 J). Figure 11f presents the η after 3600 s of solar irradiation. rGO/N-CQD$_{60/40}$ exhibited the highest efficiency (82.64%), followed by GO (65.73%), N-CQD (53.41%), and DI water (40.37%). The photothermal conversion performance of rGO/N-CQD$_{60/40}$ nanofluid under varying solar light intensities (2 and 3 Suns) was investigated. As illustrated in Figure 11g, the nanofluid temperature increased with higher light intensity, reaching 15.47, 22.85, and 25.95 °C at 1, 2, and 3 Suns, respectively. However, the η decreased with increasing intensity (Figure 11h), achieving 82.64, 66.73, and 51.11% at 1, 2, and 3 Suns, respectively, with the highest efficiency observed at 1 Sun. Although higher radiation intensity raises the temperature, heat dissipation and absorption saturation constrain further photothermal conversion. While increased sunlight intensity boosts heat storage (eq 9), the gain is disproportionately lower than the increased input energy, indicating substantial energy losses. Mechanistic explanation for the efficiency drop at higher intensities is saturation of photothermal absorption. Nanofluids have a finite light absorption capacity.[75] Beyond a certain threshold, the nanofluid cannot absorb more sunlight, and the increased input energy is largely lost instead of being converted into heat. This makes DASC systems suitable for low-intensity sunlight areas.

To evaluate photothermal conversion stability, repeated heating and cooling cycles were performed on a 0.0500%w rGO/N-CQD$_{60/40}$ nanofluid under 1000 W/m^2 light irradiation. As shown in Figure 12a, the rGO/N-CQD$_{60/40}$ nanofluid exhibited consistent temperature increases (maximum >15.47 °C) over five cycles, followed by natural cooling to room temperature. The nanofluid's absorption spectrum remained largely unchanged after each cycle, with no significant decrease in absorption or visible changes in the spectrum, indicating minimal nanoparticle aggregation (Figure S8). Furthermore, the solar-weighted absorption fractions at a penetration depth of 1.5 cm exhibited a low standard deviation (0.0251) across cycles, confirming the thermal stability of the nanofluid during repeated heating and cooling (Figure 12b). These consistent heating and cooling curves demonstrate the reliable photothermal conversion stability and remarkable performance of the nanofluid, especially over extended durations.

4. CONCLUSIONS

A composite of 2D nanostructures (rGO) and 0D functional nanocarbon (N-CQD) was synthesized via a mild hydrothermal method at varying ratios to evaluate the photothermal performance in direct absorption solar collectors (DASCs). Nanofluids were prepared using a two-step method, and physicochemical characterization revealed that rGO/N-CQD$_{60/40}$ nanofluid exhibited the highest thermal conductivity (TC) and remained stable for 18 days. Characterization via UV−vis, FTIR, Raman, XRD, XPS, EDAX, AFM, and TEM confirmed that a 40/60 ratio of N-CQDs to rGO nanosheets yielded an optimal structure and morphology, making it a suitable candidate for DASCs. Optical property analysis showed that the rGO/N-CQD$_{60/40}$ nanofluid had the lowest transmittance and the highest extinction coefficient. At a 1 cm penetration depth, solar radiation absorption was significantly higher for rGO/N-CQD$_{60/40}$ (97.97%) compared with DI water (7.32%), N-CQD (35.32%), and GO (74.77%). Photothermal studies at 1 Sun intensity demonstrated efficiencies of 40.37, 53.41, 65.73, and 82.64% for DI water, N-CQD, GO, and rGO/N-CQD60/40, respectively, highlighting the potential of the rGO/N-CQD$_{60/40}$ nanofluid for DASCs due to its dispersion stability, solar absorption, and photothermal conversion. Investigation of solar energy absorption and efficiency under varying solar radiation intensities (1−3 Suns) revealed peak performance at the lowest intensity (1 Sun), indicating effective solar energy utilization even under low radiation. Finally, an artificial neural network with six neurons in the hidden layer and Tan-Sig and Purelin transfer functions accurately predicted the thermal conductivity of rGO/N-CQD$_{60/40}$ (R^2 = 0.9974).

■ ASSOCIATED CONTENT

Data Availability Statement

The raw/processed data required to reproduce these findings cannot be shared presently as the data also forms part of an ongoing study.

SI Supporting Information

The Supporting Information is available free of charge at https://pubs.acs.org/doi/10.1021/acsaem.5c00938.

Experimental setup; results of sedimentation of different nanofluids; the TC, TCR, and TCE% of different nanofluids; the obtained TC from the experimental and ANN model, comparing the ANN output with experimental data; the average absorptivity of different nanofluids; the infrared thermographs of different nanofluids, key technical parameters for DT-980; the energy absorbed by different nanofluids; and UV−vis absorption spectra after each heating−cooling cycle (PDF)

AUTHOR INFORMATION

Corresponding Author

Mohammad H. Entezari − *Sonochemical Research Center, Department of Chemistry, Ferdowsi University of Mashhad, Mashhad 917794897, Iran; Environmental Chemistry Research Center, Department of Chemistry, Ferdowsi University of Mashhad, Mashhad 917794897, Iran;* orcid.org/0000-0003-2918-4221; Email: moh_entezari@yahoo.com, entezari@um.ac.ir

Author

Mahbobeh Javidi − *Sonochemical Research Center, Department of Chemistry, Ferdowsi University of Mashhad, Mashhad 917794897, Iran*

Complete contact information is available at: https://pubs.acs.org/10.1021/acsaem.5c00938

Notes

The authors declare no competing financial interest.

ACKNOWLEDGMENTS

Support from the Ferdowsi University of Mashhad (Research and Technology) for this work (Code No. 3/59594) is appreciated.

REFERENCES

(1) Gorji, T. B.; Ranjbar, A. A. A Review on Optical Properties and Application of Nanofluids in Direct Absorption Solar Collectors (DASCs). *Renewable Sustainable Energy Rev.* **2017**, *72*, 10−32.

(2) Shahbaz, M.; Nwani, C.; Bekun, F. V.; Gyamfi, B. A.; Agozie, D. Q. Discerning the Role of Renewable Energy and Energy Efficiency in Finding the Path to Cleaner Consumption and Production Patterns: New Insights from Developing Economies. *Energy* **2022**, *260*, No. 124951.

(3) Kumar Verma, S.; Kumar, R.; Barthwal, M.; Rakshit, D. A Review on Futuristic Aspects of Hybrid Photo-Voltaic Thermal Systems (PV/T) in Solar Energy Utilization: Engineering and Technological Approaches. *Sustainable Energy Technol. Assess.* **2022**, *53*, No. 102463.

(4) Luo, X.; Shi, J.; Zhao, C.; Luo, Z.; Gu, X.; Bao, H. The Energy Efficiency of Interfacial Solar Desalination. *Appl. Energy* **2021**, *302*, No. 117581.

(5) Lewis, N. S. Research Opportunities to Advance Solar Energy Utilization. *Science* **2016**, *351* (6271), No. aad1920.

(6) Bandarra Filho, E. P.; Mendoza, O. S. H.; Beicker, C. L. L.; Menezes, A.; Wen, D. Experimental Investigation of a Silver Nanoparticle-Based Direct Absorption Solar Thermal System. *Energy Convers. Manage.* **2014**, *84*, 261−267.

(7) Javidi, M.; Entezari, M. H. The Effect of Ultrasonic Waves on the Structure, Morphology, and Thermal Conductivity of Graphene Oxide as Nanofluids for Direct Absorption Solar Collector Application. *Renewable Energy* **2024**, *237*, No. 121683.

(8) Hachicha, A. A.; Said, Z. Numerical Modeling and Multi-Objective Optimization of Direct Absorption Solar Collectors Using Mono and Hybrid Nanofluids. *J. Cleaner Prod.* **2023**, *414*, No. 137740.

(9) Brzóska, K.; Golba, A.; Kuczak, M.; Mrozek-Wilczkiewicz, A.; Boncel, S.; Dzida, M. Bio-Based Nanofluids of Extraordinary Stability and Enhanced Thermal Conductivity as Sustainable Green Heat Transfer Media. *ACS Sustainable Chem. Eng.* **2021**, *9* (21), 7369−7378.

(10) De los Santos, D.; Gallardo, J. J.; Carrillo-Berdugo, I.; Alcántara, R.; Estellé, P.; Gragera, S.; Gragera, M.; Navas, J. Nanofluids Based on Pd Nanoparticles and a Linear Silicone-Based Fluid: Toward Highly Efficient Heat Transfer Fluids for Concentrated Solar Power. *ACS Sustainable Chem. Eng.* **2024**, *12* (6), 2375−2385.

(11) Wan, M.; Xu, B.; Shi, L.; Zhou, T.; Zheng, N.; Sun, Z. Self-Assembled Au-CQDs Nanofluids with Excellent Solar Absorption and Medium−High Temperature Stability for Solar Energy Harvesting. *J. Colloid Interface Sci.* **2024**, *672*, 765−775.

(12) Chen, X.; Ye, Q.; Shi, C.; Zhang, L.; Zhou, P.; Chen, M. Understanding Solar Thermal Gradient to Improve Solar Evaporation Performance for Water Collection. *Nano Res. Energy* **2025**, *4*, No. e9120152.

(13) Swapna, M. N. S.; Korte, D.; Sankararaman, S. I. Solid-Volume-Fraction Retained Tailoring of Thermal Diffusivity of Multiwalled Carbon Nanotube Nanofluid: A Photothermal Investigation. *Phys. Status Solidi A* **2023**, *220* (5), No. 2200797.

(14) Wang, K.; He, Y.; Kan, A.; Yu, W.; Wang, L.; Wang, D.; Liu, P.; Xie, H.; She, X. Enhancement of Therminol-Based Nanofluids with Reverse-Irradiation for Medium-Temperature Direct Absorption Solar Collection. *Mater. Today Energy* **2020**, *17*, No. 100480.

(15) Haeri, S. Z.; Dashan, A.; Sadeghi, S.; Golgoli, M.; Khiadani, M.; Ramezanzadeh, B.; Zargar, M. Photo-Thermal Conversion Properties of MXene/Metal-Organic-Frameworks-Based Nanofluids for Solar Energy Harvesting. *J. Colloid Interface Sci.* **2025**, *683*, 150−165.

(16) Slepičková Kasálková, N.; Slepička, P.; Švorčík, V. Carbon Nanostructures, Nanolayers, and Their Composites. *Nanomaterials* **2021**, *11* (9), 2368.

(17) Shen, X.; Song, J.; Kawakami, K.; Ariga, K. Zero to Zero Nanoarchitectonics with Fullerene: From Molecules to Nanoparticles. *J. Nanopart. Res.* **2023**, *25* (3), No. 45.

(18) Rudyak, V. Y.; Dashapilov, G. R.; Minakov, A. V.; Pryazhnikov, M. I. Comparative Characteristics of Viscosity and Rheology of Nanofluids with Multi-Walled and Single-Walled Carbon Nanotubes. *Diamond Relat. Mater.* **2023**, *132*, No. 109616.

(19) Rao, C. N. R.; Sood, A. K.; Subrahmanyam, K. S.; Govindaraj, A. Graphene: The New Two-Dimensional Nanomaterial. *Angew. Chem., Int. Ed.* **2009**, *48* (42), 7752−7777.

(20) Allen, M. J.; Tung, V. C.; Kaner, R. B. Honeycomb Carbon: A Review of Graphene. *Chem. Rev.* **2010**, *110* (1), 132−145.

(21) Alexander, K.; Sheshrao Gajghate, S.; Shankar Katarkar, A.; Majumder, A.; Bhaumik, S. Role of Nanomaterials and Surfactants for the Preparation of Graphene Nanofluid: A Review. *Mater. Today Proc.* **2021**, *44*, 1136−1143.

(22) Tan, J.; Wang, X.; Hou, W.; Zhang, X.; Liu, L.; Ye, J.; Wang, D. Fabrication of Fe3O4@graphene/TiO2 Nanohybrid with Enhanced Photocatalytic Activity for Isopropanol Degradation. *J. Alloys Compd.* **2019**, *792*, 918−927.

(23) Shejale, K. P.; Jaiswal, A.; Kumar, A.; Saxena, S.; Shukla, S. Nitrogen Doped Carbon Quantum Dots as Co-Active Materials for Highly Efficient Dye Sensitized Solar Cells. *Carbon* **2021**, *183*, 169−175.

(24) Herold, F.; Imhof, T.; Roumeliotis, P.; Schühle, P.; Ledendecker, M.; Rønning, M. Controlled Doping of Carbon Catalyst Supports by Atomic Replacement via Gasification-Assisted Heteroatom Doping. *Carbon* **2023**, *207*, 207−218.

(25) Chen, X.; Xiong, Z.; Chen, M.; Zhou, P. Ultra-Stable Carbon Quantum Dot Nanofluids for Direct Absorption Solar Collectors. *Sol. Energy Mater. Sol. Cells* **2022**, *240*, No. 111720.

(26) Chen, X.; Wu, D.; Zhou, P.; Chen, M.; Yan, H. Modeling the Solar Absorption Performance of Copper@Carbon Core−Shell Nanoparticles. *J. Mater. Sci.* **2021**, *56* (24), 13659−13672.

(27) Chen, X.; Chen, M.; Zhou, P. Solar-Thermal Conversion Performance of Heterogeneous Nanofluids. *Renewable Energy* **2022**, *198*, 1307−1317.

(28) Kim, C. B.; Lee, J.; Cho, J.; Goh, M. Thermal Conductivity Enhancement of Reduced Graphene Oxide via Chemical Defect Healing for Efficient Heat Dissipation. *Carbon* **2018**, *139*, 386−392.

(29) Chen, M.; Zou, C.; Tang, W.; Huang, Y.; Sun, H. Experimental and Modeling Studies of N-Doped Carbon Quantum Dot Nanofluids

for Heat Transfer Systems. *Diamond Relat. Mater.* **2022**, *129*, No. 109394.

(30) Prado, J. I.; Calviño, U.; Lugo, L. Experimental Methodology to Determine Thermal Conductivity of Nanofluids by Using a Commercial Transient Hot-Wire Device. *Appl. Sci.* **2022**, *12* (1), 329.

(31) Ajeena, A. M.; Farkas, I.; Víg, P. A Comparative Experimental Study on Thermal Conductivity of Distilled Water-Based Mono Nanofluids with Zirconium Oxide and Silicon Carbide for Thermal Industrial Applications: Proposing a New Correlation. *Int. J. Thermofluids* **2023**, *20*, No. 100424.

(32) Shahrul, I. M.; Mahbubul, I. M.; Khaleduzzaman, S. S.; Saidur, R.; Sabri, M. F. M. A Comparative Review on the Specific Heat of Nanofluids for Energy Perspective. *Renewable Sustainable Energy Rev.* **2014**, *38*, 88−98.

(33) Li, L.; Rong, S.; Wang, R.; Yu, S. Recent Advances in Artificial Intelligence and Machine Learning for Nonlinear Relationship Analysis and Process Control in Drinking Water Treatment: A Review. *Chem. Eng. J.* **2021**, *405*, No. 126673.

(34) Jawad, J.; Hawari, A. H.; Javaid Zaidi, S. Artificial Neural Network Modeling of Wastewater Treatment and Desalination Using Membrane Processes: A Review. *Chem. Eng. J.* **2021**, *419*, No. 129540.

(35) Rostami, S.; Nadooshan, A. A.; Raisi, A.; Bayareh, M. Modeling the Thermal Conductivity Ratio of an Antifreeze-Based Hybrid Nanofluid Containing Graphene Oxide and Copper Oxide for Using in Thermal Systems. *J. Mater. Res. Technol.* **2021**, *11*, 2294−2304.

(36) ÇOlak, A. B. A Novel Comparative Investigation of the Effect of the Number of Neurons on the Predictive Performance of the Artificial Neural Network: An Experimental Study on the Thermal Conductivity of ZrO2 Nanofluid. *Int. J. Energy Res.* **2021**, *45* (13), 18944−18956.

(37) Zang, H.; Cheng, L.; Ding, T.; Cheung, K. W.; Wang, M.; Wei, Z.; Sun, G. Application of Functional Deep Belief Network for Estimating Daily Global Solar Radiation: A Case Study in China. *Energy* **2020**, *191*, No. 116502.

(38) Chen, H.-L.; Huang, C.-C.; Yu, X.-G.; Xu, X.; Sun, X.; Wang, G.; Wang, S.-J. An Efficient Diagnosis System for Detection of Parkinson's Disease Using Fuzzy k-Nearest Neighbor Approach. *Expert Syst. Appl.* **2013**, *40* (1), 263−271.

(39) Gouda, S. G.; Hussein, Z.; Luo, S.; Yuan, Q. Model Selection for Accurate Daily Global Solar Radiation Prediction in China. *J. Cleaner Prod.* **2019**, *221*, 132−144.

(40) Yu, W.; Xie, H. A Review on Nanofluids: Preparation, Stability Mechanisms, and Applications. *J. Nanomater.* **2012**, *2012*, 1−17.

(41) Sarsam, W. S.; Amiri, A.; Kazi, S. N.; Badarudin, A. Stability and Thermophysical Properties of Non-Covalently Functionalized Graphene Nanoplatelets Nanofluids. *Energy Convers. Manage.* **2016**, *116*, 101−111.

(42) Drotning, W. D. Optical Properties of Solar-Absorbing Oxide Particles Suspended in a Molten Salt Heat Transfer Fluid. *Sol. Energy* **1978**, *20* (4), 313−319.

(43) Zhu, W.; Zuo, X.; Ding, Y.; Yan, H.; An, Y.; Yang, W. Experimental Investigation on the Photothermal Conversion Performance of Cuttlefish Ink Nanofluids for Direct Absorption Solar Collectors. *Appl. Therm. Eng.* **2023**, *221*, No. 119835.

(44) Li, X.; Zou, C.; Chen, W.; Lei, X. Experimental Investigation of β-Cyclodextrin Modified Carbon Nanotubes Nanofluids for Solar Energy Systems: Stability, Optical Properties and Thermal Conductivity. *Sol. Energy Mater. Sol. Cells* **2016**, *157*, 572−579.

(45) Yu, X.; He, G.; Wu, J.; Wu, Z.; Wang, Y.; Dong, L.; Xie, H. Enhancement of Solar-to-Thermal Properties of Multiple-Point Cu2O/TiN Plasmonic Nanofluids. *Chem. Eng. J.* **2024**, *498*, No. 155523.

(46) Zhou, J.; Li, X.; Chen, W.; Cui, R.; Wu, X. Investigation on the Photothermal Performance of Carbon Quantum Dots Nanofluid with High-Stability. *Diamond Relat. Mater.* **2022**, *128*, No. 109233.

(47) Wang, H.; Li, X.; Luo, B.; Wei, K.; Zeng, G. The MXene/Water Nanofluids with High Stability and Photo-Thermal Conversion for Direct Absorption Solar Collectors: A Comparative Study. *Energy* **2021**, *227*, No. 120483.

(48) Wen, J.; Chang, Q.; Zhu, J.; Cui, R.; He, C.; Yan, X.; Li, X. The Enhanced Photothermal Characteristics of Plasmonic ZrC/TiN Composite Nanofluids for Direct Absorption Solar Collectors. *Renewable Energy* **2023**, *206*, 676−685.

(49) Li, X.; Zeng, G.; Lei, X. The Stability, Optical Properties and Solar-Thermal Conversion Performance of SiC-MWCNTs Hybrid Nanofluids for the Direct Absorption Solar Collector (DASC) Application. *Sol. Energy Mater. Sol. Cells* **2020**, *206*, No. 110323.

(50) Shen, J.; Shi, M.; Ma, H.; Yan, B.; Li, N.; Hu, Y.; Ye, M. Synthesis of Hydrophilic and Organophilic Chemically Modified Graphene Oxide Sheets. *J. Colloid Interface Sci.* **2010**, *352* (2), 366−370.

(51) Aladesuyi, O. A.; Oluwafemi, O. S. Synthesis of Glutamine-Based Green Emitting Carbon Quantum Dots as a Fluorescent Nanoprobe for the Determination of Iron (Fe3+) in Solanum Tuberrosum (Potato). *Heliyon* **2023**, *9* (5), No. e15904.

(52) Zhang, Y.; Ma, H.-L.; Zhang, Q.; Peng, J.; Li, J.; Zhai, M.; Yu, Z.-Z. Facile Synthesis of Well-Dispersed Graphene by γ-Ray Induced Reduction of Graphene Oxide. *J. Mater. Chem.* **2012**, *22* (26), 13064.

(53) Al-Gaashani, R.; Najjar, A.; Zakaria, Y.; Mansour, S.; Atieh, M. A. XPS and Structural Studies of High Quality Graphene Oxide and Reduced Graphene Oxide Prepared by Different Chemical Oxidation Methods. *Ceram. Int.* **2019**, *45* (11), 14439−14448.

(54) Huang, Y.; Ma, E.; Zhao, G. Thermal and Structure Analysis on Reaction Mechanisms during the Preparation of Activated Carbon Fibers by KOH Activation from Liquefied Wood-Based Fibers. *Ind. Crops Prod.* **2015**, *69*, 447−455.

(55) López-Díaz, D.; López Holgado, M.; García-Fierro, J. L.; Velázquez, M. M. Evolution of the Raman Spectrum with the Chemical Composition of Graphene Oxide. *J. Phys. Chem. C* **2017**, *121* (37), 20489−20497.

(56) Xie, L.; Ling, X.; Fang, Y.; Zhang, J.; Liu, Z. Graphene as a Substrate To Suppress Fluorescence in Resonance Raman Spectroscopy. *J. Am. Chem. Soc.* **2009**, *131* (29), 9890−9891.

(57) Wang, P.; Zhang, D.; Zhang, L.; Fang, Y. The SERS Study of Graphene Deposited by Gold Nanoparticles with 785nm Excitation. *Chem. Phys. Lett.* **2013**, *556*, 146−150.

(58) Kim, T. Y.; Park, C.-H.; Marzari, N. The Electronic Thermal Conductivity of Graphene. *Nano Lett.* **2016**, *16* (4), 2439−2443.

(59) Krishnamoorthy, K.; Veerapandian, M.; Yun, K.; Kim, S.-J. The Chemical and Structural Analysis of Graphene Oxide with Different Degrees of Oxidation. *Carbon* **2013**, *53*, 38−49.

(60) Lu, S.; Guo, S.; Xu, P.; Li, X.; Zhao, Y.; Gu, W.; Xue, M. Hydrothermal Synthesis of Nitrogen-Doped Carbon Dots with Real-Time Live-Cell Imaging and Blood−Brain Barrier Penetration Capabilities. *Int. J. Nanomed.* **2016**, *Volume 11*, 6325−6336.

(61) Qiu, J.; Liao, J.; Wang, G.; Du, R.; Tsidaeva, N.; Wang, W. Implanting N-Doped CQDs into RGO Aerogels with Diversified Applications in Microwave Absorption and Wastewater Treatment. *Chem. Eng. J.* **2022**, *443*, No. 136475.

(62) Rong, M.; Feng, Y.; Wang, Y.; Chen, X. One-Pot Solid Phase Pyrolysis Synthesis of Nitrogen-Doped Carbon Dots for Fe3+ Sensing and Bioimaging. *Sensors Actuators B Chem.* **2017**, *245*, 868−874.

(63) John, B. K.; John, N.; Korah, B. K.; Thara, C.; Abraham, T.; Mathew, B. Nitrogen-Doped Carbon Quantum Dots as a Highly Selective Fluorescent and Electrochemical Sensor for Tetracycline. *J. Photochem. Photobiol. A Chem.* **2022**, *432*, No. 114060.

(64) Madbouly, L. A.; Mrkwitschka, P.; Stockmann, J. M.; Jones, E.; Radnik, J.; Hodoroaba, V. Comparative Elemental Analysis of Commercial Functionalized Graphene Nanoplatelets Along the Production Chain With X-Ray Photoelectron and Energy-Dispersive X-Ray Spectroscopy. *Surf. Interface Anal.* **2025**, *57* (4), 300−306.

(65) Kubota, R.; Tanaka, W.; Hamachi, I. Microscopic Imaging Techniques for Molecular Assemblies: Electron, Atomic Force, and Confocal Microscopies. *Chem. Rev.* **2021**, *121* (22), 14281−14347.

(66) Chakraborty, S.; Panigrahi, P. K. Stability of Nanofluid: A Review. *Appl. Therm. Eng.* **2020**, *174*, No. 115259.

(67) Mahian, O.; Kianifar, A.; Kalogirou, S. A.; Pop, I.; Wongwises, S. A Review of the Applications of Nanofluids in Solar Energy. *Int. J. Heat Mass Transfer* **2013**, *57* (2), 582−594.

(68) Lu, Z.; Yin, Y. Colloidal Nanoparticle Clusters: Functional Materials by Design. *Chem. Soc. Rev.* **2012**, *41* (21), 6874.

(69) Ahmed, W.; Zaman Chowdhury, Z.; Kazi, S. N.; Johan, M. R. Bin.; Badruddin, I. A.; Soudagar, M. E. M.; Kamangar, S.; Mujtaba, M. A.; Gul, M.; Khan, T. M. Y. Evaluation on Enhanced Heat Transfer Using Sonochemically Synthesized Stable Zno-Eg@Dw Nanofluids in Horizontal Calibrated Circular Flow Passage. *Energies* **2021**, *14* (9), 2400.

(70) Hadadian, M.; Goharshadi, E. K.; Youssefi, A. Electrical Conductivity, Thermal Conductivity, and Rheological Properties of Graphene Oxide-Based Nanofluids. *J. Nanopart. Res.* **2014**, *16* (12), No. 2788.

(71) Younes, H.; Mao, M.; Sohel Murshed, S. M.; Lou, D.; Hong, H.; Peterson, G. P. Nanofluids: Key Parameters to Enhance Thermal Conductivity and Its Applications. *Appl. Therm. Eng.* **2022**, *207*, No. 118202.

(72) Stauffer, D.; Aharony, A. *Introduction To Percolation Theory*; Taylor & Francis, 2018. DOI: 10.1201/9781315274386.

(73) Gao, J.; Yu, W.; Xie, H.; Mahian, O. Graphene-Based Deep Eutectic Solvent Nanofluids with High Photothermal Conversion and High-Grade Energy. *Renewable Energy* **2022**, *190*, 935−944.

(74) Li, Z.; Kan, A.; Wang, K.; He, Y.; Zheng, N.; Yu, W. Optical Properties and Photothermal Conversion Performances of Graphene Based Nanofluids. *Appl. Therm. Eng.* **2022**, *203*, No. 117948.

(75) Yu, J.; Wang, Y.; Qi, C.; Zhang, W. Photothermal and Photoelectric Properties of Ag@Fe3O4 Nanofluids. *Sol. Energy Mater. Sol. Cells* **2023**, *258*, No. 112434.